

## Laboratory Model Tests and DEM Simulations of Unloading-Induced Tunnel Failure Mechanism

Abierdi<sup>1</sup>, Yuzhou Xiang<sup>2</sup>, Haiyi Zhong<sup>2</sup>, Xin Gu<sup>2</sup>, Hanlong Liu<sup>2,3</sup> and Wengang Zhang<sup>2,3,\*</sup>

**Abstract:** Tunnel excavation is a complicated loading-unloading-reloading process characterized by decreased radial stresses and increased axial stresses. An approach that considers only loading, is generally used in tunnel model testing. However, this approach is incapable of characterizing the unloading effects induced by excavation on surrounding rocks and hence presents radial and tangential stress paths during the failure process that are different from the actual stress state of tunnels. This paper carried out a comparative analysis using laboratory model testing and particle flow code (PFC<sup>2D</sup>)-based numerical simulation, and shed light upon the crack propagation process and, microscopic stress and force chain variations during the loading-unloading process. The failure mode observed in the unloading model test is shear failure. The force chains are strongly correlated with the concrete fracture propagation. In addition, the change patterns of the radial and tangential stresses of surrounding rocks in the broken region, as well as the influence of the initial stress on failure loads are revealed. The surrounding soil of tunnel failure evolution as well as extent and shape of the damage zone during the excavation-induced unloading were also studied.

**Keywords:** Tunnel, unloading, model testing, particle flow model, force chain.

### 1 Introduction

Due to the massive transportation construction over the past few years, tunnel engineering in China has experienced unprecedented development, which also poses more stringent technical requirements on the plan, design and construction of tunnels. Tunnel excavation is accompanied by stress re-distribution in the surrounding rock masses, tunnel convergence, and possibly, tunnel instability and failure. Tunnel instability and the consequent failure are the most critical issue for engineers, and understanding the mechanics behind tunnel excavation is of great significance. Many valuable studies have been carried out all over the world, and the current research methodology mainly includes the model testing [Idinger, Aklik and Wu (2011); Wong, Ng and Chen (2012); Lin, Liu and Zhou (2015); Divall and

---

<sup>1</sup> School of Hehai, Chongqing Jiaotong University, Chongqing, 400074, China.

<sup>2</sup> School of Civil Engineering, Chongqing University, Chongqing, 400045, China.

<sup>3</sup> Key Laboratory of New Technology for Construction of Cities in Mountain Area, Chongqing University, Chongqing, 400045, China.

\* Corresponding Author: Wengang Zhang. Email: cheungwg@126.com.

Received: 14 July 2019; Accepted: 19 August 2019.

Goodey (2012); Ahmed and Iskander (2011); Xiang, Liu, Zhang et al. (2018)], field instrumentation [Zhang and Huang (2014); Palazzo (2014); Kontogianni, Tzortzis and Stiros (2004)], numerical simulation [Rabczuk and Belytschko (2004); Jia and Tang (2008); Chen, Tang and Ling (2011); Wang, Sloan and Sheng (2012); Wang, Sloan and Tang (2012); Wilson, Abbo and Sloan (2013); Li, Zhang and Fang (2014); Zhang and Goh (2015); Fagnoli, Gragnano and Boldini (2015); Areias, Msekh and Rabczuk (2016); Ren, Zhuang and Rabczuk (2017); He, Li and Li (2017); Aswin and Chang (2017); Ali, Lyamin and Huang (2017); Avgerinos, Potts and Standing (2017); Paternesi, Schweiger and Scarpelli (2017); Areias, Reinoso, Camanho et al. (2018); Goh, Zhang, Zhang et al. (2018); Zhou, Rabczuk and Zhuang (2018); Zhou, Zhuang, Zhu et al. (2018); Zhou, Zhuang and Rabczuk (2019); Chen, Wang and Zhang (2019)], and analytical solution [Liu and Yuan (2015); Zhao, Li and Li (2017); Mollon, Dias and Soubra (2010); Lü, Xiao and Ji (2017); Liang, Xia and Hong (2016); Gue and Wilcock (2017)]. Model testing has been proven in practice as an effective method in underground engineering.

Underground excavation is a complex loading-unloading process. So far, most studies assume an overloading process of first excavation and subsequent loading to investigate the tunnel failure pattern, and yet the revealed in-situ stress state and variation of the displacement field in the failure process are different from the actual unloading process in tunnel excavation. Thus these references fail to reveal the unloading effect induced by excavation on surrounding rocks. Overloading-based studies on tunnel excavation are to some extent limited, as for true embodiment of disturbance in stresses and strains during tunnel excavation. For model testing, it is capable of both qualitatively and quantitatively characterizing the load and deformation features of tunnel surrounding rocks, and provides references for analyses on tunnel failure mechanisms. Given the aforementioned research gaps, this paper carried out experimental testing of loading and unloading in tunnel excavation, and corresponding numerical simulation using PFC<sup>2D</sup>, a Discrete Element Method (DEM)-based software, to illustrate the evolution of the stress, strain and failure plane in the unloading process of tunnel excavation and mechanism behind such phenomena. The findings of this research shed insights into the unloading-induced stress and strain variations in tunnel excavation, and contribute to the guidance on the tunnel design and construction.

## **2 Laboratory model testing of tunnel excavation**

### **2.1 Strength measurements**

To reduce the effects of material heterogeneity on testing results, the model was made up of a single type of gypsum mixed with water. The mass ratio of gypsum to water was 2:0.5. Uniaxial compression testing and Brazilian split testing were carried out to determine the tension-compression (T-C) ratio of gypsum, using computer-controlled constant loading compression testing machine, as shown in Fig. 1. Testing results are summarized in Tabs. 1 and 2. The uniaxial compressive strength (UCS) and tensile strength of gypsum are 2.804 MPa and 0.213 MPa, respectively. As the exerted load reached the peak value during the uniaxial compressive testing, the gypsum sample broke instantly with a clear sound, indicating obvious brittleness.



(a) Uniaxial compression testing samples (b) Brazilian split testing samples

**Figure 1:** Gypsum failure in T-C measurements

**Table 1:** Results of uniaxial compression testing

Material	No.	Peak Load/kN	Fracture Angle $f/^\circ$	Specimen Dimension $\Phi \times H/\text{mm}$	UCS $\sigma_{cu}/\text{MPa}$	Average UCS $\sigma_{cu}/\text{MPa}$
Gypsum	1	2.82	61	39.2×80	2.337	2.804
	2	3.63	69	39.2×80	3.008	
	3	3.58	63	39.2×80	2.966	
	4	3.54	63	39.2×80	2.933	
	5	3.35	63	39.2×80	2.776	

**Table 2:** Results of Brazilian split testing

Material	No.	Peak Load /kN	Specimen Dimension $a \times b \times H/\text{mm}$	Tensile Strength $\sigma_{cu}/\text{MPa}$	Average Tensile Strength $\sigma_{cu}/\text{MPa}$
Gypsum	1	3.49	100×100×100	0.222	0.213
	2	3.20	100×100×100	0.204	
	3	3.35	100×100×100	0.213	

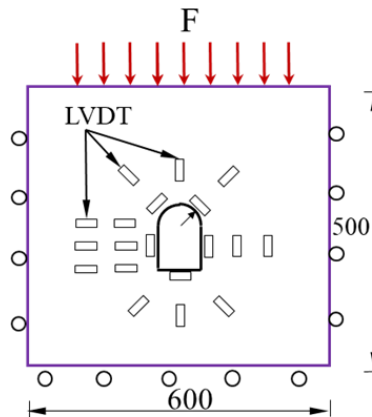
The shear mechanical parameters of gypsum were measured via laboratory tests and results are shown in Tab. 3.

**Table 3:** Physical and mechanical parameters of gypsum

Material	Young's Modulus $E/\text{MPa}$	Poisson's Ratio $\nu/1$	Specific Weight $P/(\text{kN}\cdot\text{m}^{-3})$	Cohesion $c/\text{MPa}$	Internal Friction Angle $\varphi/^\circ$	T-C Ratio $/1$
Gypsum	40.95	0.20	17.8	0.312	30.0	13.16

### 2.2 Experimental conditions

The loading apparatus used in the test was the WE-600B hydraulic universal testing machine which is capable of meeting the requirements of applying load to complex model, with the maximum axial load of 600 kN. The test simulated the failure process of tunnels during unloading. To this end, a tunnel testing model has been fabricated, the dimensions of which were 60 cm×500 cm×15 cm, as shown in Fig. 2. Steel plates were first fixed according to design, as illustrated in Fig. 3. Then gypsum and water were mixed rapidly and thoroughly by the given ratio, after which the model was filled with the mixture in a layer-by-layer manner. Each layer was about 8 cm thick and vibrated before working on the next layer. After 15 days of curing time, the material strength grew to the required value for testing. Strain gauges, used to record the strain variation during the loading/unloading process, were then fixed to the model surface. Plane strain constraints were imposed upon the model, which means the steel plates in the front, back left and right were fixed with no displacement variation. The vertical load  $\sigma_z$  was evenly exerted on the top surface of the model by the hydraulic universal testing machine, and as for the lateral load,  $\sigma_x=\sigma_y=\nu/(1+\nu)\times\sigma_z$ .

**Figure 2:** Dimensions of the testing model (units in mm)



**Figure 3:** Fixed steel plates and the testing boundary conditions

### **3 Unloading failure testing**

#### ***3.1 Fracture propagation in the failure process***

Unloading tests reveal the stress-strain evolution during the unloading-induced failure process of tunnels as well as the failure plane growth and failure mechanism. In order to determine the in-situ stress of surrounding rocks during unloading, the load, at which the tunnel first breaks down in the overloading testing, was defined as the initial surrounding rock pressure of the unloading testing. As the vertical stress reaches 1.167 MPa, rock pieces drop off from the foots of the two side walls, and fractures initiate, propagate obliquely upward to the spandrel and finally evolve into a semicircle sliding plane. Therefore, it can be concluded that the peak load with respect to first breakage of the model was about 1.167 MPa, as shown in Fig. 4, which was then defined as the initial surrounding rock pressure in the unloading testing.

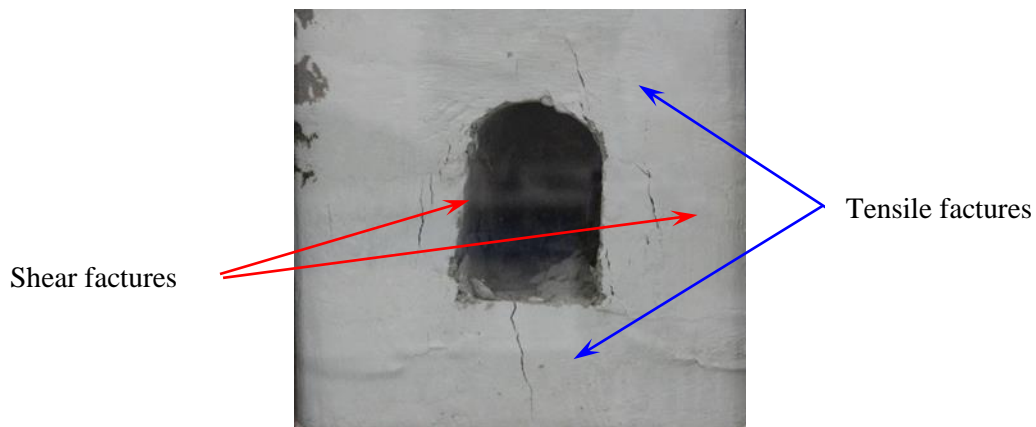
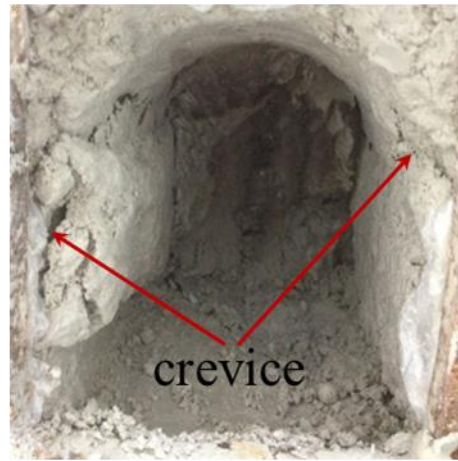


**Figure 4:** Overloading failure of the tunnel model, at the vertical stress of 1.167 MPa

Before excavation, the model is intact, as shown in Fig. 5(a) with no notable cracks in the surrounding rock. The vertical stress rose up to 1.167 MPa, then excavation started from one side of the model and gradually penetrated towards the other side. As two thirds of the tunnel was excavated, inclined fractures occurred at the left spandrel, and vertical fracture penetration showed on the left side wall, which led to rock extrusion (seen in Fig. 5(b)). While excavation proceeds, the right side wall extruded and fell off, and upward-inclined fractures occurred at the feet of both side walls and gradually propagated. Upon completion of the tunnel, it was observed that the two vertical side walls were greatly pushed inward. The whole tunnel was stable, as the failure plane growth stopped (Fig. 5(c)).



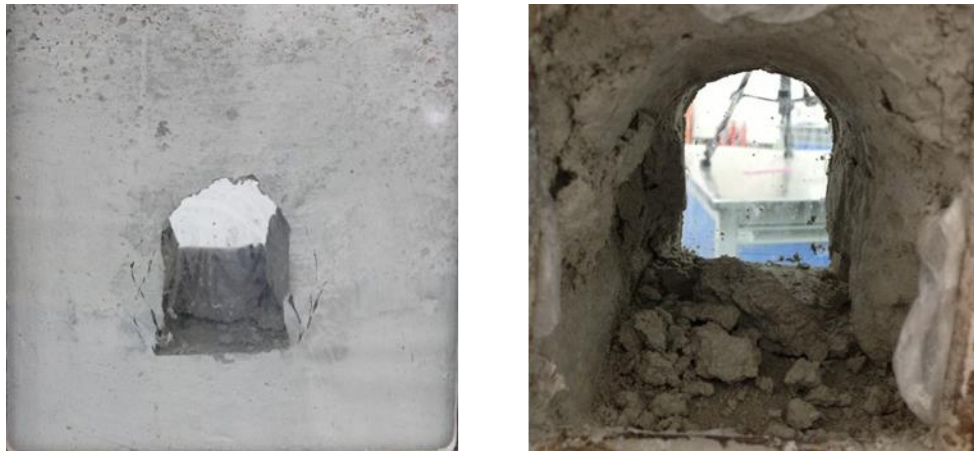
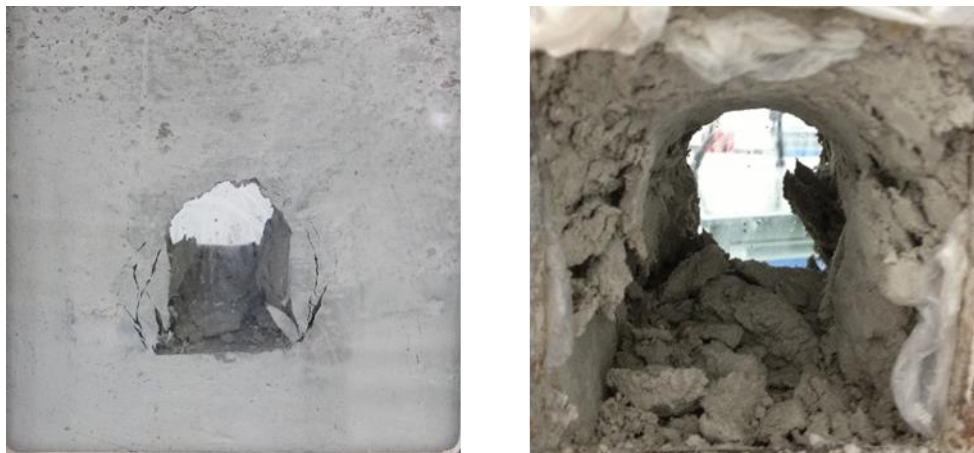
(a)  $\sigma_z=0$  MPa~1.167 MPa, before excavation.



(b)  $\sigma_z=1.167$  MPa, during excavation.



(c)  $\sigma_z=1.167$  MPa, excavation completed.

(d)  $\sigma_z=1.333$  MPa(e)  $\sigma_z=1.417$  Mpa**Figure 5:** Fracture propagation with loading in gypsum tunnel model testing

In order to examine the failure evolution of tunnels, loading imposed on top of the model was increased. When  $\sigma_z$  reached 1.333 MPa, the left side wall extruded, with several new vertical fractures appearing in the sliding body, and fractures on right side penetrated from the foot of the wall to the spandrel, with climbing crack depths. It was concluded as the first breaking down of the model. As the load continued to grow, a whole collapse occurred on the left side wall, and the failed loosen area of surrounding rocks expanded. The surrounding soil body extruded toward the free face, and the tunnel size decreased.

The unloading failure plane in tunnel excavation is shown in Fig. 6. It is seen that during excavation of the model imposed by certain load, micro cracks initiate at the foot of wall, and propagate obliquely upward deep into the surrounding rock, as the excavation proceeds. This results in broken soil bodies on side walls, moving toward the free face, and great compressive deformation of the model. With load approaching a certain value, fractures at the wall foot and spandrel connect with each other and cause a big semicircle spall. The depth of the left crack was about 3.0 cm, and that of the right crack was 2.9 cm. The pattern

of unloading failure during excavation of the gypsum model was shear failure.

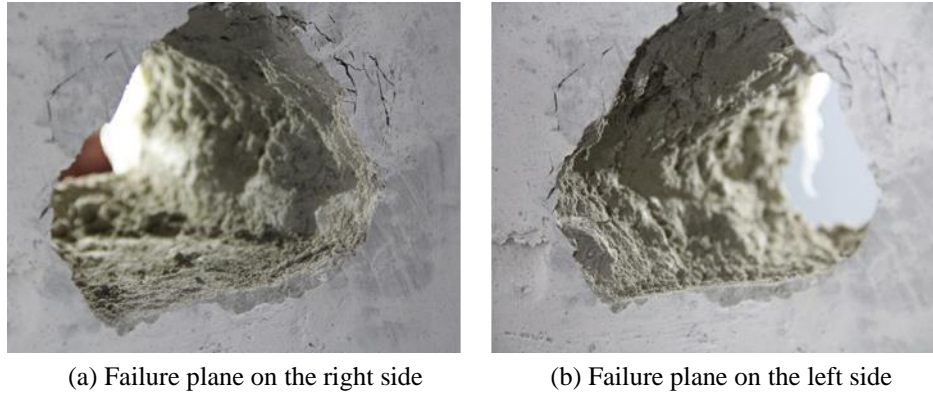


**Figure 6:** Failure planes of the gypsum tunnel model

### 3.2 Stress-strain evolution

The radial and tangential strains at each measuring spot on the tunnel model side wall was recorded during the unloading process of tunnel excavation. The layout of strain gauges on the testing model is shown in Fig. 7 and the tangential strain versus vertical stress at each measuring spot is plotted in Figs. 8 and 9. Fig. 8 indicates that tangential strains at each measuring point on the tunnel sidewall all slightly change with variations in loading, before excavation. After the initial surrounding rock pressure reaches the given value, excavation begins and still tangential strains only show limited increments. This suggests that the vertical deformation is relatively small during tunnel excavation. With the excavation accomplished and loading continuously increased, the strain at each measuring point gradually rises. With a vertical stress of about 1.333 MPa, an uprush is seen in the measured strain, which means the tunnel sidewall is subjected to the first breakage. As the loading continues, strains at each point increasingly fluctuate, and the tunnel was further destructed.

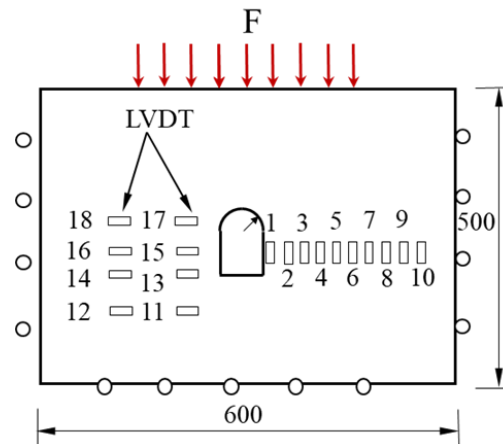


**Figure 7:** Layout of strain gauges on the testing model

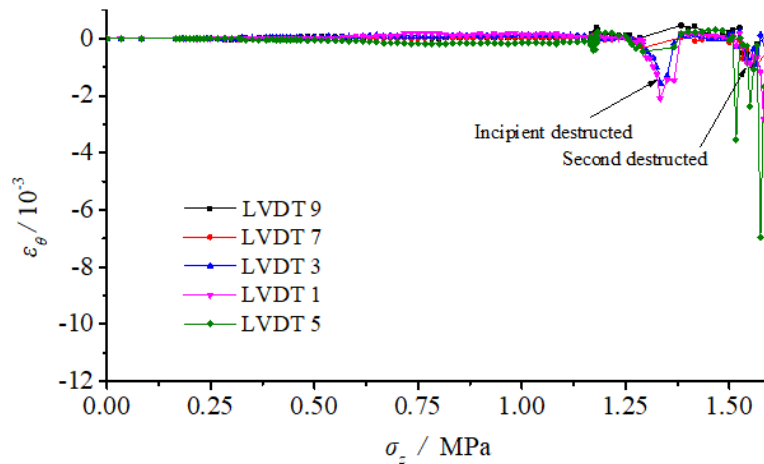


**Figure 8:** Tangential strain vs. vertical load at each measuring spot on the tunnel model sidewall

Fig. 9 shows that with vertical load on top of the model  $\sigma_z$  reaching 1.167 MPa ( $P_z=70$  kN), tensile strains at sidewall measuring points are about  $1.0 \times 10^{-3}$ - $1.5 \times 10^{-3}$ . As excavation starts to penetrate through the model from one side, the vertical load is kept constant and the tensile strains at Spots 11, 12 and 13 (Spot 13>Spot 12>Spot 11) continuously grow, which implies horizontal inward deformation of the tunnel induced by tensile stresses of sidewalls. Moreover, the tensile strain grows with a position approaching the center of the sidewall, and this is consistent to the observation in Fig. 5(c). With continuing loading after excavation, radial strains further increase.

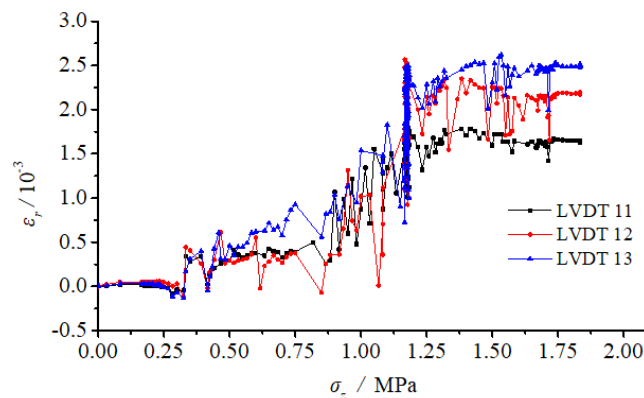


**Figure 9:** Radial strain vs. vertical load at measuring points around the tunnel

According to the strain data, it is safe to say that the excavation-induced unloading forces the tunnel sidewalls to deform towards the free face, and vertical walls are subjected to tensile stresses and fractured at last. Before tunnel failure, the vertical subsidence deformation is relatively small, and in cases of failure, vertical subsidence considerably accelerates, with fast growing strains. Semicircle sliding planes are formed and result in

collapse of the entire structure. The peak load with reference to the excavation unloading failure of the model  $\sigma_{z\max}$  is 1.333 MPa ( $P_{z\max}=80$  kN).

#### 4 Discrete element method (DEM)-based analyses

A particle flow model, with dimensions identical to those of the actual model, was built using FISH (a programming language) in PFC<sup>2D</sup> simulation, in order to compare the tunnel model testing and PFC-based numerical simulation. The simulation model was simplified into a plane-strain model. Constraints were applied to the left and right walls and the bottom surface, and servo-controlled overloading was imposed on the top surface of the model, which leads to fine simulation of the testing process. For DEM simulation, the determination of microscopic parameters is critical and directly impacts the accuracy of the DEM calculation. This paper, on the basis of comparison between mechanical parameters based on laboratory pseudo-triaxial and numerical triaxial tests, as well as back analysis, thoroughly investigated the corresponding effects of each microscopic parameter of the parallel bonded model on the macroscopic mechanics and shed light upon the interaction between parameters, with only one single factor changing at a time. The final values of the microscopic parameters are shown in Tab. 4.

**Table 4:** PFC Microscopic parameters

Porosity $n/\%$	16
Minimum particle size $R_{min}/\text{mm}$	0.30
Radius ratio $R_{max}/R_{mi}$	1.66
Particle density $\rho_b$ ( $\text{kg}/\text{m}^3$ )	2 976
Particle contact modulus $E_c/\text{GPa}$	23.0
Particle stiffness ratio $k_n/k_s(I)$	2.63
Friction coefficient $\mu/I$	0.40
Bonding radius multiplier $\bar{\lambda}/I$	1.0
Parallel bond modulus $E_c/\text{GPa}$	25.0
Parallel bond stiffness ratio $k_n/k_s(I)$	2.73
Normal bonding strength $\bar{\sigma}_c/\bar{\sigma}_{cs}$ (MPa)	60/16
Tangential bonding strength $\bar{\tau}_c/\bar{\tau}_{cs}$ (MPa)	70/16

##### 4.1 Stress-strain evolution

The damage zone development, corresponding to the excavation unloading testing after the vertical stress exerted on surrounding rocks of the gypsum tunnel  $\sigma_z$  has risen up to a constant value of 1.167 MPa ( $P_z=70$  kN), as illustrated in Fig. 10, in which no notable cracks are observed prior to excavation. After excavation initiated, the vertical stress was kept at 1.167 MPa during the numerical iteration. At Iteration Step 1000, damages occurred at the foots of sidewalls and spandrels of the tunnel model as well as deep regions of vertical walls. As iteration proceeded, cracks at the sidewall foot propagated obliquely

upward into the deep surrounding, and meanwhile fractures at the spandrel extended obliquely downward. In addition, a small amount of particles fell off from the free face. When iteration reached Step 2500, fractures from the sidewall foots and spandrel have joined each other. With continuing iteration, the crack width at the sliding plane further expanded, and the damaged zone at the vertical walls moved toward the deep surrounding and created a larger failure plane.

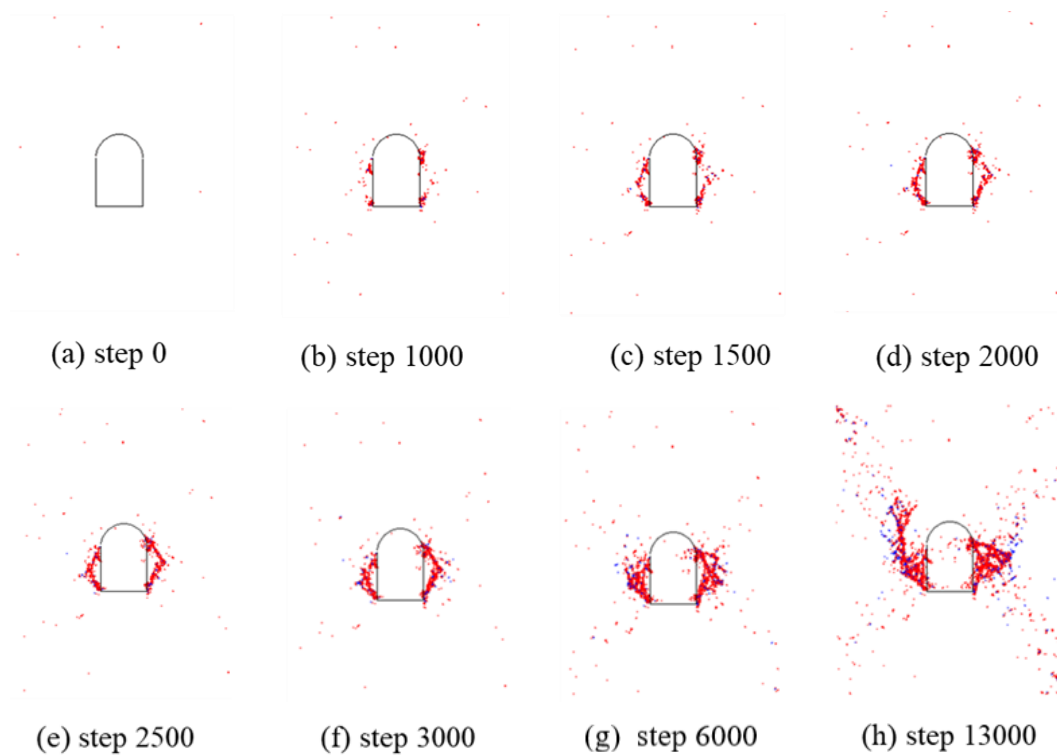


**Figure 10:** Damage evolution of the gypsum tunnel unloading testing

The failure plane of the tunnel model in the laboratory test is compared with that of the numerical simulation, as is shown in Fig. 11. In terms of the failure mode, excavation-induced unloading breaks the soil body of the tunnel side wall, which is then forced to displace toward the free face. Cracks at the foots of sidewalls and spandrels propagate and connect with each other, which finally forms a sliding fall-off. In the laboratory modeling test, the initiation of excavation under loading of 1.167 MPa only generates a few cracks, without overall failure. A sliding plane penetrating through the surrounding rock does not occur until the loading further increases to 1.333 MPa. The sliding plane is accompanied by multiple intersected fractures, with damage zones of 2.9 cm-3.0 cm depth. In cases of numerical simulation, tunnel failure occurs at the beginning of the excavation under the surrounding rock pressure of 1.167 MPa. The sliding body is relatively intact, with influence zone of 2.6 cm-2.9 cm depth. The laboratory and numerical tests are of the similar failure modes, and present consistent failure plane evolution patterns and ranges. However, the failure load is different in magnitudes, which can be mainly attributed to the fact that the

material strength is constant for numerical simulation while the gypsum strength in the model test is increased via the compaction effect induced by vibration. Generally speaking, it is safe to draw conclusion that PFC, capable of well capturing the unloading failure process during tunnel excavation, is a good alternative for laboratory model testing.

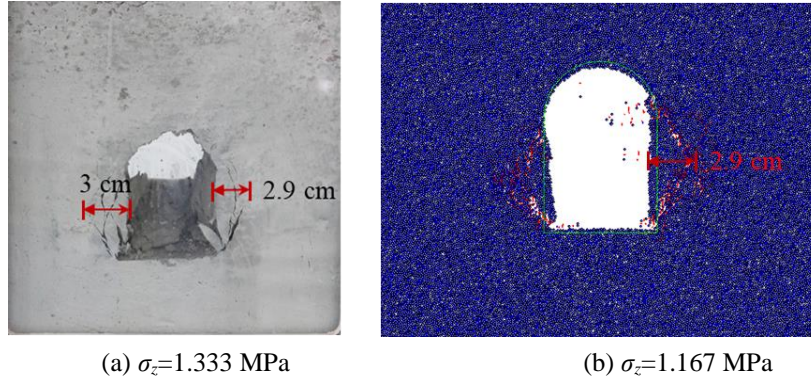
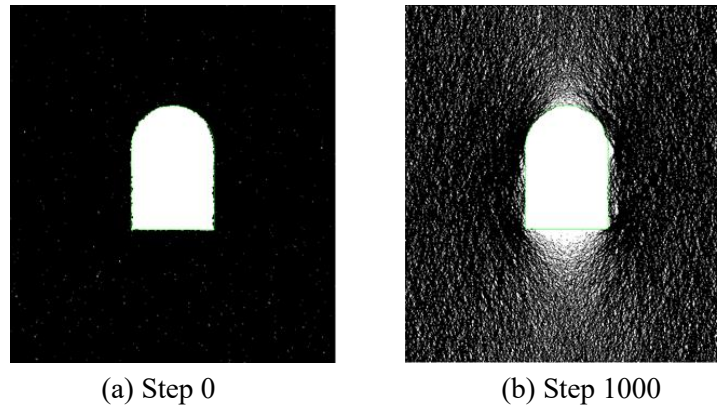


**Figure 11:** Failure plane comparison of the tunnel model unloading testing

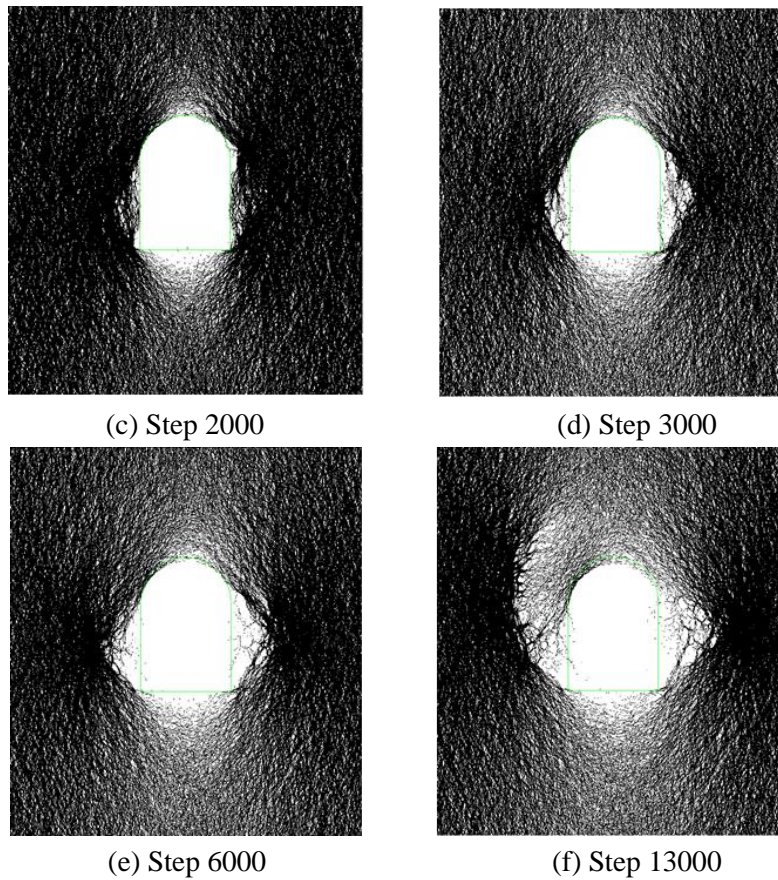
#### 4.2 Stress-strain evolution pattern

The force chain distribution of the gypsum tunnel loaded by 1.167 MPa is presented in Fig. 12. It is indicated the force chain distribution is relatively even prior to unloading, with the maximum contact loading of 3.69 kN. As excavation proceeds, the strong force chain is located at the free face. Pressure arching occurs at the crown and bottom of the tunnel, with 1000 times of iteration and stresses concentrate at the foots of sidewalls and spandrels, which generates a maximum contact force of 4.56 kN, damages the foots of sidewalls and spandrels, and turns the strong force chain toward the deep surrounding. The broken zones of surrounding rocks on the two vertical sidewalls further expand with the advancing iteration. At Iteration Step 2500, the broken depth of the two sidewalls is about 2.2 cm. For Step 6000, it increases to 3.4 cm, but the arch crown and bottom are relatively stable with no notable expansion of the pressure arch.



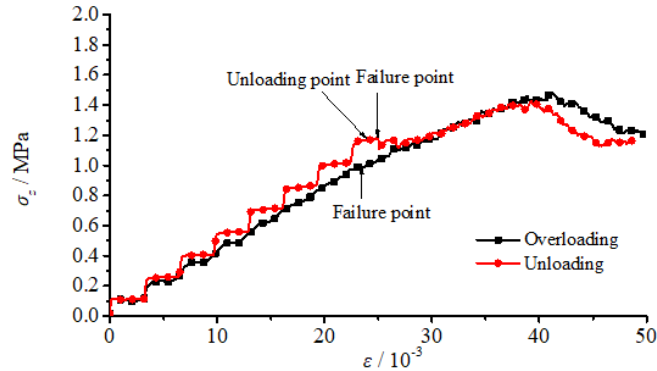
(a) Step 0

(b) Step 1000



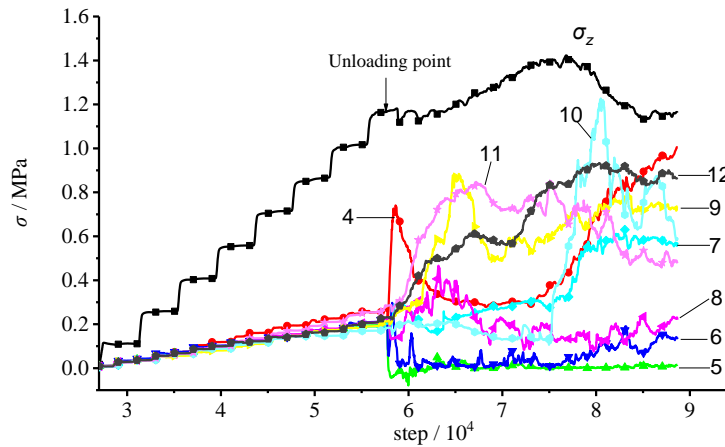
**Figure 12:** Force chain distribution in the tunnel unloading testing (kN)

Fig. 13 shows the correlation between load and deformation of the model, in which the black line represents the overloading testing result while the red one denotes the unloading testing result. In the initial stress applying stage of the unloading testing, the stress on roof presents wavelike rise and a nearly linear correlation with the strain. After excavation starts, the stress is almost stable and at mean times, the strain grows. A stress drop is observed at the first appearance of penetrating fractures (failure). The stress-strain curve then rises again, with a lower slope, mainly because that a new profile of the tunnel has been created after surrounding rocks on the two vertical sidewalls fall off and greater load is required for further failure. As the load further grows, the stress-strain curve gradually deflects from the linear elasticity. At last, it reaches the peak and then falls in a curved manner.



**Figure 13:** Comparison of correlations between load and deformation

The stress variation captured by the measuring element on the vertical wall is plotted in Fig. 14. It is found that during the gradual loading of the initial stress, the stress at each measuring spot increases linearly with the load imposed on the model surface. The vertical (tangential) stress  $\sigma_\theta$  is equal to the stress exerted on the model surface  $\sigma_z$ , and the horizontal (radial) stress is lower, with  $\sigma_r : \sigma_z : \sigma_\theta = 0.21 : 1.0 : 1.0$ . When the load reaches 1.167 MPa, excavation begins. The radial stress at Point 4 grows rapidly to the peak value of 0.74 MPa and then falls down. Moreover, measured radial stresses at Points 5 and 6 quickly decrease to zero, and tangential stresses at Points 4, 5 and 6 also decreases to relatively lower values. This reflects the significant unloading effects induced by excavation unloading on the free face. As the unloading process initiates, tangential and radial stresses at Points 7, 8 and 9 all to some extent rise, which implies that no failure occurs at these positions at the beginning of the unloading. Then with 500 times of iteration, the radial stress at Point 8 reaches the peak value ( $\sigma_r = 0.466$  MPa, and  $\sigma_\theta = 1.80$  MPa). Then the radial stress at Point 9 got the maximum value at Iteration Step 770 ( $\sigma_r = 0.884$  MPa, and  $\sigma_\theta = 1.90$  MPa), and gradually declines afterwards, indicating that the broken zone of surrounding rocks expands. As iteration proceeds, the measuring points located in deeper surrounding arrive at the peak stress one after another, and the broken range of surrounding rocks continuously expands.



(a) Radial stress

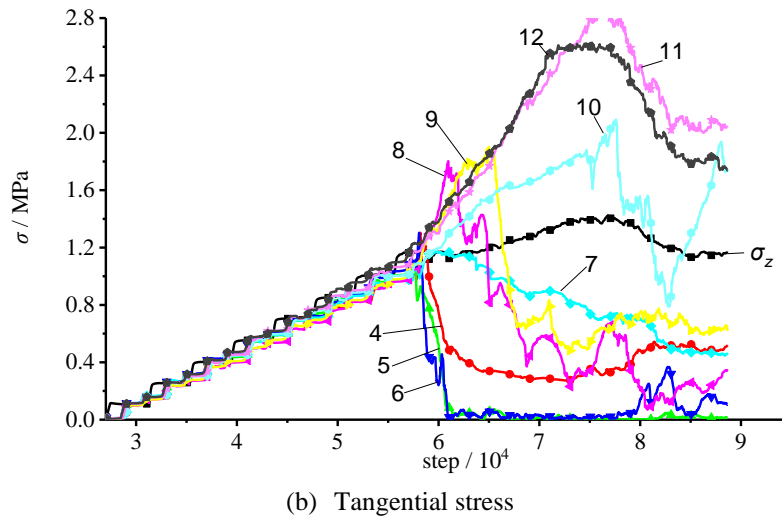
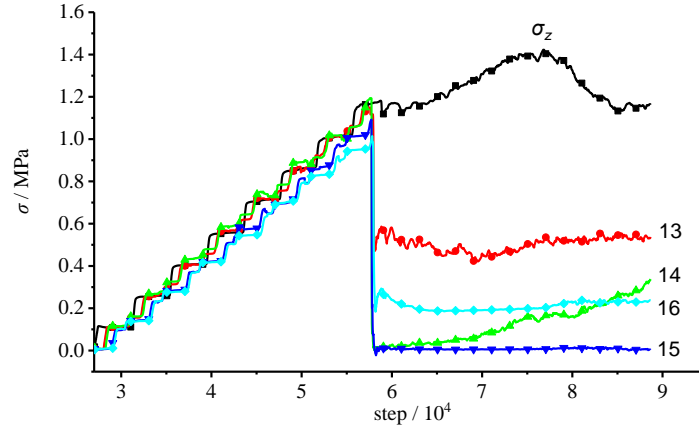


**Figure 14:** Stress variation of the measuring element on the vertical wall during tunnel excavation

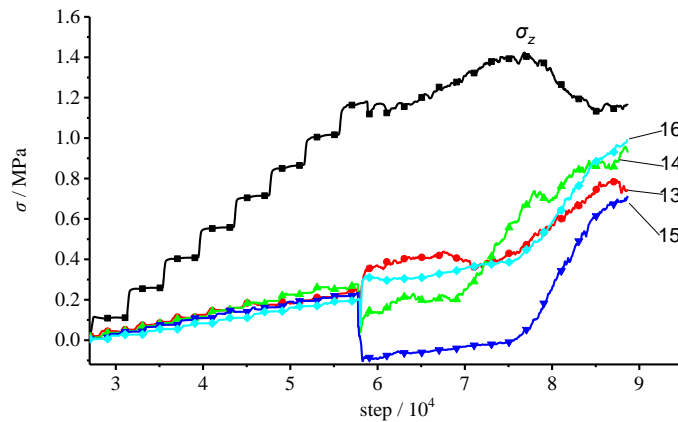
From the elastoplastic point of view, the radial stress of the tunnel surrounding rock falls down and meanwhile the tangential stress should increase. However, the particle flow modelling demonstrates that stress concentration occurs around the free face, following the tunnel excavation and contributing to strong force chain effects. The radial and tangential stresses of the surrounding rock both increase, and this breaks the surrounding rock. The surrounding rock in the broken range is loosened, and therefore both of the radial and tangential stresses decline. The strong force chain moves toward the deeper surrounding region, which rapidly raises up the radial and tangential stresses of deeper surrounding rock and further expands the broken range.

The unloading-induced stress variations recorded by measuring elements at the arch crown and bottom during the tunnel excavation are illustrated in Fig. 15. It indicated that during the process of applying the initial stress, stresses at each measuring point are identical and linearly increase. The vertical (radial) stress  $\sigma_\theta$  equals to the imposed load  $\sigma_z$ , and the horizontal (tangential) stress is lower than the former two, with  $\sigma_r : \sigma_z : \sigma_\theta = 0.21 : 1.0 : 1.0$ . In the scenario of the on-going tunnel excavation after the stress increases to 1.167 MPa, the radial stresses at points 13-16 quickly drop to relatively low values. The radial stresses at inner measuring elements 13 and 16 are higher than those of surface measuring elements 14 and 15. The radial stress at Spot 13 decreases to about 0.53 MPa, while for Spot 16 to 0.21 MPa or so, respectively by 55% and 82%. The radial stress at each measuring element is basically constant afterwards. This indicates that during the whole process, the loading states of the arch crown and bottom are relatively stable. As for tangential stresses, rapid drops of tangential stresses are observed at points 14 and 15, and point 15 at the arch bottom are even transformed from the compressive state ( $\sigma_\theta = 0.235$  MPa) into the tensile state ( $\sigma_\theta = -0.104$  MPa). For Points 13 and 16, the tangential stress firstly increases and then basically stays stable during the subsequent iteration. This also suggests that the loading states of the arch crown and bottom are relatively stable during the whole excavation process.

Nevertheless, certain tensile stresses are generated at the arch bottom, which means that during tunnel excavation, the inverted arch should be built in time, for safety considerations.



(a) Radial stress



(b) Tangential stress

**Figure 15:** Stress variations at measuring elements at the arch crown and bottom during unloading

With continuous loading after the primary failure of the surrounding rock of the tunnel, the tangential stresses of the measuring elements at the tunnel roof and base reach their inflection points and grow sharply, leading to the overall instability and failure of the tunnel model.

## 5 Conclusions

On the basis of the comparison between the lab model test and PFC<sup>2D</sup>-based numerical simulations, the follow conclusions have been drawn:

- (1) The failure mode observed in the unloading model test is shear failure, in which the two vertical sidewalls extruded toward the free face. The unloading deformation of surrounding rocks toward the free face is relatively small, but the damage depth is higher. The failure mode presented in the numerical simulation is consistent with that in model test. Therefore, the particle flow modelling can be used to simulate tunnel failure.

- (2) As excavation proceeds, pressure arching occurs at the crown and bottom while stress concentrations occur at the sidewall foot and spandrel, resulting in the maximum contact force chain. The strong force chain moves toward the deeper surrounding, which further expands the broken region.
- (3) The stress in the damaged region decreases fast while the influential zone rapidly expands. The disturbance stress induced by tunnel excavation grows with the initial stress. Therefore, with higher initial stresses, the failure load of the tunnel reduces and the tunnel becomes more prone to failure. After unloading failure, the post-peak stress of surrounding rocks falls even faster, which contributes to the catastrophic characteristics of unloading-induced failure.

It should be noted that the results of the physical model test are constrained by the model sizes and dimensions while the numerical simulation results are limited by the plane-strain assumption. It should also be noted that an uncertainty analysis as done in Hamdia et al. [Hamdia, Silani, Zhuang et al. (2017)] would be conducted in the future research, which is of great engineering practice to civil engineers.

**Acknowledgement:** The authors are grateful to the support by the National Natural Science Foundation of China (No. 51608071), Natural Science Foundation of Chongqing, China (cstc2018jcyjAX0632), General Financial Grant from the China Postdoctoral Science Foundation (Grant No. 2017M620414) and the Special Funding for Post-doctoral Researchers in Chongqing (No. Xm2017007).

**Conflicts of Interest:** The authors declare that they have no conflicts of interest to report regarding the present study.

## References

- Ahmed, M.; Iskander, M.** (2011): Analysis of tunneling-induced ground movements using transparent soil models. *Journal of Geotechnical and Geoenvironmental Engineering*, vol. 137, no. 5, pp. 525-535.
- Ali, A.; Lyamin, A. V.; Huang, J.** (2017): Undrained stability of a single circular tunnel in spatially variable soil subjected to surcharge loading. *Computers and Geotechnics*, vol. 84, no. 1, pp. 16-27.
- Areias, P.; Msekh, M. A.; Rabczuk, T.** (2016). Damage and fracture algorithm using the screened Poisson equation and local remeshing. *Engineering Fracture Mechanics*, vol. 158, pp. 116-143.
- Areias, P.; Reinoso, J.; Camanho, P. P.; de Sá, J. C.; Rabczuk, T.** (2018): Effective 2D and 3D crack propagation with local mesh refinement and the screened Poisson equation. *Engineering Fracture Mechanics*, vol. 189, pp. 339-360.
- Aswin, L.; Ou, C. Y.** (2017): Stress paths in deep excavations under undrained conditions and its influence on deformation analysis. *Tunnelling and Underground Space Technology*, vol. 63, no. 1, pp. 118-132.
- Avgerinos, V.; Potts, D. M.; Standing, J. R.** (2017): Numerical investigation of the effects

of tunnelling on existing tunnels. *Géotechnique*, vol. 67, no. 9, pp. 808-822.

**Chen, F. Y.; Wang, L.; Zhang, W. G.** (2019): Reliability assessment on stability of tunneling perpendicularly beneath an existing tunnel considering spatial variabilities of rock mass properties. *Tunnelling and Underground Space Technology*, vol. 88, pp. 276-289.

**Chen, R. P.; Tang, L. J.; Ling, D. S.** (2011): Face stability analysis of shallow shield tunnels in dry sandy ground using the discrete element method. *Computers and Geotechnics*, vol. 38, no. 1, pp. 187-195.

**Divall, S.; Goodey, R. J.** (2012): Apparatus for centrifuge modelling of twin-tunnel construction. *International Journal of Physical Modelling in Geotechnics*, vol. 12, no. 3, pp. 102-111.

**Fargnoli, V.; Gragnano, C. G.; Boldini, D.** (2015): 3D numerical modelling of soil-structure interaction during EPB tunnelling. *Géotechnique*, vol. 65, no. 1, pp. 23-37.

**Goh, A. T.; Zhang, W. G.; Zhang, Y. M.; Xiao, Y.; Xiang, Y. Z.** (2018): Determination of EPB tunnel-related maximum surface settlement: a multivariate adaptive regression splines approach. *Bulletin of Engineering Geology and the Environment*, vol. 77, pp. 489-500.

**Gue, C. Y.; Wilcock, M. J.; Alhaddad, M. M.** (2017): Tunnelling close beneath an existing tunnel in clay-perpendicular undercrossing. *Géotechnique*, vol. 67, no. 9, pp. 795-807.

**Hamdia, K. M.; Silani, M.; Zhuang, X. Y.; He, P.; Rabczuk, T.** (2017): Stochastic analysis of the fracture toughness of polymeric nanoparticle composites using polynomial chaos expansions. *International Journal of Fracture*, vol. 206, no. 2, pp. 215-227.

**He, P.; Li, S. C.; Li, L. P.** (2017): Discontinuous deformation analysis of super section tunnel surrounding rock stability based on joint distribution simulation. *Computers and Geotechnics*, vol. 91, no. 1, pp. 218-229.

**Idinger, G.; Aklik, P.; Wu, W.** (2011): Centrifuge model test on the face stability of shallow tunnel. *Acta Geotechnica*, vol. 6, no. 2, pp. 105-117.

**Jia, P.; Tang, C. A.** (2008): Numerical study on failure mechanism of tunnel in jointed rock mass. *Tunnelling and Underground Space Technology*, vol. 23, no. 1, pp. 500-507.

**Kontogianni, V.; Tzortzis, A.; Stiros, S.** (2004): Deformation and failure of the tymfristos tunnel, Greece. *Journal of Geotechnical and Geoenvironmental Engineering*, vol. 130, no. 10, pp. 1004-1113.

**Li, Y.; Zhang, D.; Fang, Q.** (2014): A physical and numerical investigation of the failure mechanism of weak rocks surrounding tunnels. *Computers and Geotechnics*, vol. 61, no. 1, pp. 292-307.

**Liang, R.; Xia, T.; Hong, Y.** (2016): Effects of above-crossing tunnelling on the existing shield tunnels. *Tunnelling and Underground Space Technology*, vol. 58, no. 1, pp. 159-176.

**Lin, P.; Liu, H.; Zhou, W.** (2015): Experimental study on failure behaviour of deep tunnels under high in-situ stresses. *Tunnelling and Underground Space Technology*, vol. 46, no. 1, pp. 28-45.

**Liu, X. Y.; Yuan, D. J.** (2015): Mechanical analysis of anti-buoyancy safety for a shield tunnel under water in sands. *Tunnelling and Underground Space Technology*, vol. 47, no. 1, pp. 153-161.

- Lü, Q.; Xiao, Z. P.; Ji, J.** (2017): Moving least squares method for reliability assessment of rock tunnel excavation considering ground-support interaction. *Computers and Geotechnics*, vol. 84, no. 1, pp. 88-100.
- Mollon, G.; Dias, D.; Soubra, A. H.** (2010): Face stability analysis of circular tunnels driven by a pressurized shield. *Journal of Geotechnical and Geoenvironmental Engineering*, vol. 136, no. 1, pp. 215-229.
- Palazzo, S.** (2014): Tunnel excavation failures and unforeseen ground conditions. *Proceedings of the Institution of Civil Engineers-Forensic Engineering*, vol. 167, no. 4, pp. 165-174.
- Paternes, A.; Schweiger, H. F.; Scarpelli, G.** (2017): Numerical analyses of stability and deformation behavior of reinforced and unreinforced tunnel faces. *Computers and Geotechnics*, vol. 88, no. 1, pp. 256-266.
- Rabczuk, T.; Belytschko, T.** (2004): Cracking particles: a simplified meshfree method for arbitrary evolving cracks. *International Journal for Numerical Methods in Engineering*, vol. 61, no. 13, pp. 2316-2343.
- Ren, H.; Zhuang, X. Y.; Rabczuk, T.** (2017): Dual-horizon peridynamics: a stable solution to varying horizons. *Computer Methods in Applied Mechanics and Engineering*, vol. 318, pp. 762-782.
- Wang, S. Y.; Sloan, S. W.; Sheng, D. C.** (2012): Numerical analysis of the failure process around a circular opening in rock. *Computers and Geotechnics*, vol. 39, no. 1, pp. 8-16.
- Wang, S. Y.; Sloan, S. W.; Tang, C. A.** (2012): Numerical simulation of the failure mechanism of circular tunnels in transversely isotropic rock masses. *Tunnelling and Underground Space Technology*, vol. 32, no. 1, pp. 231-244.
- Wilson, D. W.; Abbo, A. J.; Sloan, S. W.** (2013): Undrained stability of a square tunnel where the shear strength increases linearly with depth. *Computers and Geotechnics*, vol. 49, no. 1, pp. 314-325.
- Wong, K. S.; Ng, C. W. W.; Chen, Y. M.** (2012): Centrifuge and numerical investigation of passive failure of tunnel face in sand. *Tunnelling and Underground Space Technology*, vol. 28, no. 1, pp. 297-303.
- Xiang, Y. Z.; Liu, H. L.; Zhang, W. G.; Chu, J.; Zhou, D. et al.** (2018): Application of transparent soil model test and DEM simulation in study of tunnel failure mechanism. *Tunnelling and Underground Space Technology*, vol. 74, pp. 178-184.
- Zhang, W. G.; Goh, A. T. C.** (2015): Numerical study of pillar stresses and interaction effects for twin rock caverns. *International Journal for Numerical and Analytical Methods in Geomechanics*, vol. 39, no. 2, pp. 193-206.
- Zhang, Z.; Huang, M.** (2014): Geotechnical influence on existing subway tunnels induced by multilane tunneling in Shanghai soft soil. *Computers and Geotechnics*, vol. 56, no. 1, pp. 121-132.
- Zhao, L.; Li, D.; Li, L.** (2017): Three-dimensional stability analysis of a longitudinally inclined shallow tunnel face. *Computers and Geotechnics*, vol. 87, no. 1, pp. 32-48.
- Zhou, S. W.; Rabczuk, T.; Zhuang, X. Y.** (2018): Phase field modeling of quasi-static and dynamic crack propagation: COMSOL implementation and case studies. *Advances in*

*Engineering Software*, vol. 122, pp. 31-49.

**Zhou, S. W.; Zhuang, X. Y.; Rabczuk, T.** (2019): Phase field modeling of brittle compressive-shear fractures in rock-like materials: a new driving force and a hybrid formulation. *Computer Methods in Applied Mechanics and Engineering*, vol. 355, pp. 729-752.

**Zhou, S. W.; Zhuang, X. Y.; Zhu, H. H.; Rabczuk, T.** (2018): Phase field modelling of crack propagation, branching and coalescence in rocks. *Theoretical and Applied Fracture Mechanics*, vol. 96, pp. 174-192.